

www.acsami.org Research Article

Radiation Resilient Two-Dimensional Electronics

Thomas F. Schranghamer, Andrew Pannone, Harikrishnan Ravichandran, Sergei P. Stepanoff, Nicholas Trainor, Joan M. Redwing, Douglas E. Wolfe, and Saptarshi Das*



Cite This: ACS Appl. Mater. Interfaces 2023, 15, 26946-26959



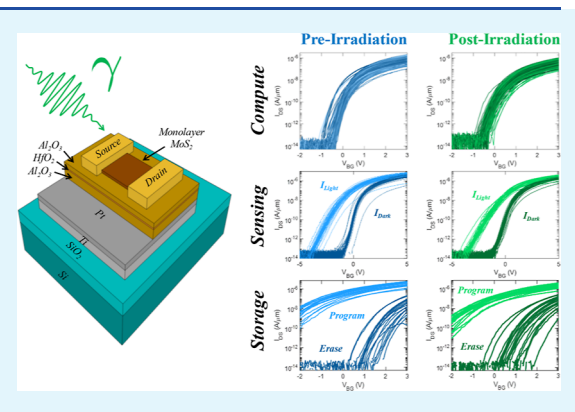
ACCESS I

III Metrics & More

Article Recommendations

s Supporting Information

ABSTRACT: Limitations in cloud-based computing have prompted a paradigm shift toward all-in-one "edge" devices capable of independent data sensing, computing, and storage. Advanced defense and space applications stand to benefit immensely from this due to their need for continual operation in areas where maintaining remote oversight is difficult. However, the extreme environments relevant to these applications necessitate rigorous testing of technologies, with a common requirement being hardness to ionizing radiation. Two-dimensional (2D) molybdenum disulfide (MoS₂) has been noted to enable the sensing, storage, and logic capabilities necessary for all-in-one edge devices. Despite this, the investigation of ionizing radiation effects in MoS₂-based devices remains incomplete. In particular, studies on gamma radiation effects in MoS₂ have been largely limited to standalone films, with few device investigations; to the best of our



knowledge, no explorations have been made into gamma radiation effects on the sensing and memory capabilities of MoS_2 -based devices. In this work, we have used a statistical approach to study high-dose (1 Mrad) gamma radiation effects on photosensitive and programmable memtransistors fabricated from large-area monolayer MoS_2 . Memtransistors were divided into separate groups to ensure accurate extraction of device characteristics pertaining to baseline performance, sensing, and memory before and after irradiation. All- MoS_2 logic gates were also assessed to determine the gamma irradiation impact on logic implementation. Our findings show that the multiple functionalities of MoS_2 memtransistors are not severely impacted by gamma irradiation even without dedicated shielding/mitigation techniques. We believe that these results serve as a foundation for more application-oriented studies going forward.

KEYWORDS: two-dimensional (2D) materials, transition metal dichalcogenides (TMDCs), MoS₂, memtransistors, logic gates, all-in-one integration, radiation hardness, gamma radiation

■ INTRODUCTION

Recent years have seen an explosive proliferation of integrated sensors and communication systems, allowing everyday electronics to capture information without human input and subsequently communicate that information between each other in the so-called Internet of things. Traditionally, these edge devices, i.e., devices lying at the network edge between information sources and their relevant datacenters, have been limited to either data producers (sensors) or data consumers, shuttling data to remote datacenters for processing and requesting information from datacenters, respectively. While effective, the rapid expansion of edge devices has caused the rate of data generation to far outstrip the ability of networks to effectively and efficiently shuttle data between devices. This, combined with other growing concerns such as the security of data uploaded from edge devices and the energy demands of transmitting/processing such vast quantities of data, has led to the investigation of all-in-one edge computing options capable of sensing, storing, and processing (computing) information without reliance on remote datacenters.^{2,3} These technologies have particular promise for defense- and space-related

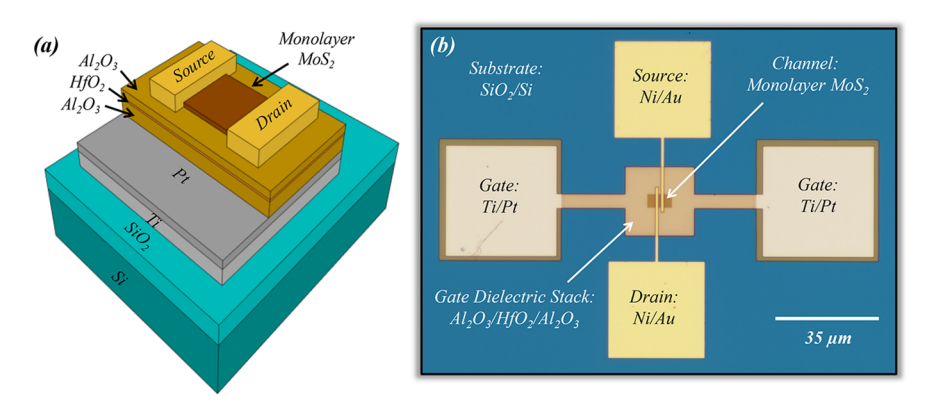
applications^{4,5} in time-sensitive environments where the remote nature of the relevant systems makes maintaining constant oversight a severe challenge.

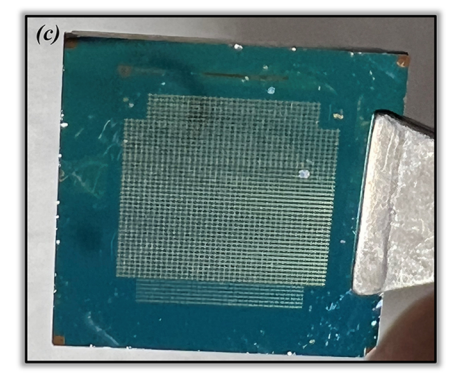
Of course, an additional hurdle for developing systems for defense- and space-related applications is that the extreme environments they operate in, *i.e.*, nuclear facilities, the upper atmosphere, low-Earth orbit (LEO), *etc.*, require special considerations. In both cases, electronic devices are expected to be resilient to damage and upsets caused by high amounts of ionizing radiation. Gamma radiation, a type of ionizing radiation which consists of extremely high-energy photons, is a particularly common concern due to its penetrative nature and prevalence in nuclear environments and in LEO. 6-8

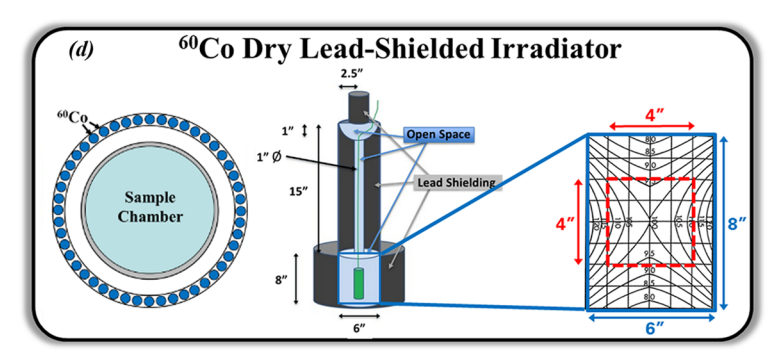
Received: February 20, 2023 Accepted: May 11, 2023 Published: May 26, 2023











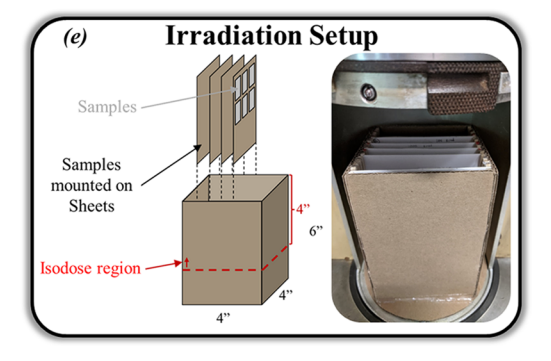


Figure 1. Overview of a two-dimensional (2D) memtransistor and experimental setup. (a) 3D schematic and (b) optical image of a representative 2D MoS_2 memtransistor used in this study. Each memtransistor consists of a Ti/Pt back-gate island, a programmable $Al_2O_3/HfO_2/Al_2O_3$ back-gate stack, and a monolayer MoS_2 channel with Ni/Au source/drain contacts. (c) Optical image of the 1 cm \times 1 cm substrate used in this study. Fabrication of a >1500 memtransistor array allowed for a thorough statistical study to be conducted on the baseline performance (computing), sensing, and memory capabilities of 2D MoS_2 memtransistors. (d) Diagram of the irradiation chamber used in this study. Irradiation occurred in a lead-shielded cylinder with a diameter of \sim 6 in. and a height of 8 in. with multiple ^{60}Co 0 sources arranged annularly around the lead-shielded chamber. (e) Varying dose rates inside the chamber necessitated the use of a custom-made paper-based sample holder to suspend the substrate within a pre-determined isodose region with a steady dose rate of \sim 160 krad/h until a total ionizing dose (TID) of 1 Mrad was reached.

Current shielding strategies and radiation-mitigating device/circuit architectures increase the cost and reduce the area/energy efficiency of electronic devices, necessitating the implementation of truly radiation-hard materials to facilitate edge device development.⁶ Note that these materials must also provide a platform capable of supporting the requirements of edge computing, namely, (1) high-performance, low-power electronic devices for computing implementation, (2) sensors with high responsivity to stimuli, and (3) memory cells for information storage between logic operations.

In this context, two-dimensional (2D) transition metal dichalcogenides (TMDCs), a class of atomically thin semiconducting materials that include molybdenum disulfide (MoS₂), display highly advantageous properties for edge computing applications. Advances in TMDC synthesis techniques and device fabrication processes have been used to demonstrate high-performance MoS, field-effect transistors (FETs);9,10 similar MoS₂ FETs have been used as the constituent units of various complex circuits, supporting highly accurate logic operations. ^{10–12} MoS₂ has also been demonstrated to be photosensitive, leading to the development of MoS₂-based photodetectors and vision systems. 12-14 Similarly, a number of memory technologies have been realized using MoS₂, including charge-trapping memories, ¹⁵ resistive memoand ferroelectric memories.¹⁷ Such a wide array of relevant applications have already led to investigations of MoS₂ for the development of all-in-one integrated platforms capable of simultaneous sensing, computing, and storage. 18 However,

the impact of radiation on these properties is still being investigated. While extensive studies have already been conducted on the impact of ion, 19-22 electron, 23-25 and proton irradiation 19,26,27 on FETs fabricated from MoS₂, similar literature pertaining to gamma irradiation is decidedly lacking. Past gamma irradiation studies have been primarily focused on the characterization of standalone MoS2 films; 7,8,28-30 while several have performed some characterization of MoS₂-based FETs, ^{7,3}1 too few devices were investigated to gain a statistical understanding of the radiation effects observed, and, to the best of our knowledge, no explorations were made into the effects of gamma irradiation on the sensing and memory capabilities of MoS₂-based devices. Thus, there remains a need for an expansive investigation of gamma irradiation effects in MoS2-based electronics across a statistically significant device population with additional consideration for radiation impact on sensing and memory.

In this work, we present a comprehensive statistical study of the effects of high-dose gamma radiation on the electrical, sensory, and memory characteristics of 2D MoS₂-based memtransistors and the accuracy of logic operations performed using MoS₂-based logic circuits. 2D memtransistors are three-terminal devices that utilize a gate terminal in conjunction with a charge-trapping gate dielectric stack to realize non-volatile and analog programming of conductance states and electrostatic control of the 2D channel. As MoS₂ is a photoactive material, illumination of the channel with light causes the generation of photocarriers, allowing for the co-location of

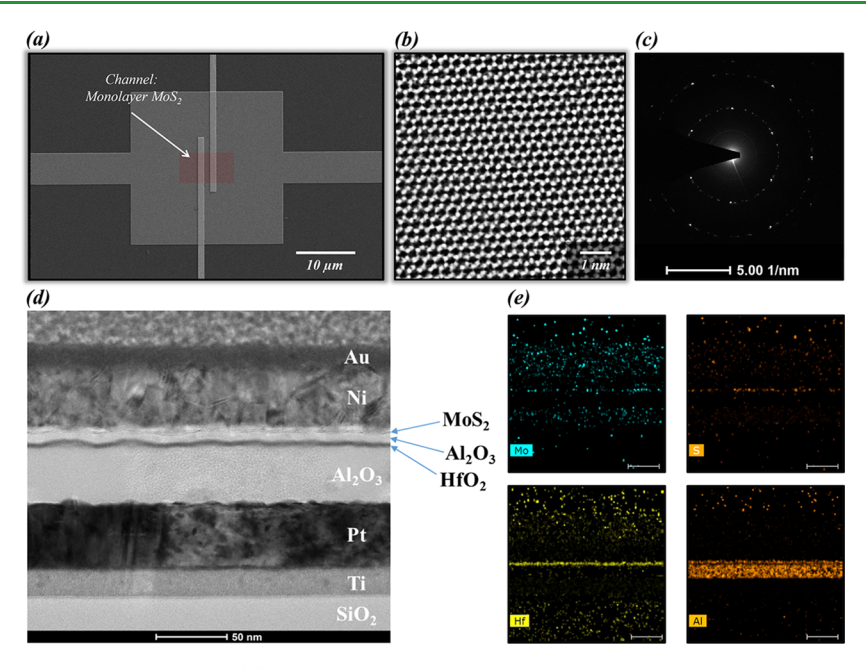


Figure 2. Electron microscopy of monolayer MoS₂. (a) Image of the channel region of a representative 2D MoS₂ memtransistor taken using a field emission scanning electron microscope at a 5 kV accelerating voltage. A red box is used to denote the MoS₂ film. (b) Atomic structure of the monolayer MoS₂ film used in this study as viewed down its *c*-axis. Image was taken at an accelerating voltage of 80 kV using an atomic resolution high-angle annular dark field-scanning transmission electron microscope. (c) Selected area electron diffraction (SAED) pattern of the MoS₂ film imaged in (b). The diffraction pattern shown indicates that the MoS₂ film possesses a uniform and single-crystalline structure. (d) Cross-sectional transmission electron microscope (TEM) image of a representative 2D MoS₂ memtransistor taken underneath the source/drain contacts following a TID of 1 Mrad. Each constituent layer is labeled. (e) Energy-dispersive X-ray spectroscopy (EDS) spectra of the elements Mo (top-left), S (top-right), Hf (bottom-left), and Al (bottom-right) for the cross-section shown in (d). Scale bars denote 90 nm. A clear line of Mo and S atoms indicates that the MoS₂ film remained coherent throughout irradiation, while the distribution of Al and Hf shows a clear delineation between the Al₂O₃ tunneling/blocking layers and the HfO₂ charge-trapping layer. Excessive signals (spots) of Mo and Hf above and below their expected distribution areas are attributed to overlapping X-ray emission peaks.

(photo)sensing with computing and memory in a single device. A 60Co source was used to irradiate both individual memtransistors and logic gates fabricated from monolayer MoS₂ grown via metal-organic chemical vapor deposition (MOCVD) for a total ionizing dose (TID) of 1 Mrad at a rate of ~160 krad/h. Raman and photoluminescence (PL) spectroscopy of the MoS₂ before and after irradiation revealed minimal change despite the gamma radiation environment being far harsher than any found in LEO (average dose rate of ~208 nrad/h).^{8,32} Electrical characterization of over 130 irradiated memtransistors showed only a slight degradation in the average subthreshold slope (SS) and field-effect mobility $(\mu_{\rm FE})$, as well as a slight shift in the average threshold voltage $(V_{\rm th})$, while the photodetection and memory capabilities of the devices were not severely impacted. The accuracy of logic operations performed using AND, NAND, NOR, XOR, and NOT gates composed of multiple connected MoS₂ memtransistors was assessed, with the irradiated gates displaying no loss in accuracy compared to their pre-irradiation states. These results indicate that MOCVD-MoS₂-based memtransistors/ circuits display impressive radiation hardness for sensing, computing, and storage applications even without dedicated shielding and mitigation techniques. Continual development of this technology, therefore, has the potential to realize edge devices/platforms capable of all-in-one sensing, computing, and storage for high radiation environments such as those found in deep space or in nuclear facilities. We believe that these results serve as a foundation for more applicationoriented studies going forward.

RESULTS

Figure 1a,b shows the schematic of the back-gated 2D MoS₂ memtransistor architecture used in this study and an optical image of a representative device, respectively. To allow for sufficient electrostatic isolation between devices for circuit fabrication, back-gating was achieved using a local back-gate island scheme. 20 nm Ti and 50 nm Pt were deposited using electron-beam (e-beam) evaporation on a commercially purchased p++-Si/SiO2 substrate to act as local back-gate electrodes. A 40 nm Al₂O₃ ($\varepsilon_{\rm ox} \approx 10$) blocking layer, a 3 nm HfO_2 ($\varepsilon_{ox} \approx 25$) charge-trapping layer, and a 7 nm Al_2O_3 tunneling layer were then sequentially deposited via atomic layer deposition (ALD) to form the back-gate dielectric stack. Similar Al₂O₃/HfO₂/Al₂O₃ stacks have been previously reported to support charge trapping/detrapping near the semiconductor/dielectric interface when gate biases of sufficient magnitude are applied, thereby allowing for the realization of non-volatile memory (NVM) states in a manner similar to traditional FLASH memories. 15,33 As will be later discussed, this phenomenon is exploited to realize NVM capabilities in the fabricated devices similar to that used in our previous works, 12,13,18,34 with the impact of gamma radiation on long-term retention and endurance being investigated. The large-area monolayer MoS2 used in this study was grown via a previously described MOCVD technique^{35,36} on an epitaxial sapphire substrate at 950 °C using carbon-free chalcogen precursors. Following growth, the film was transferred to the local back-gate island substrate using a wet transfer process³ for device fabrication. The channel of each device ($W = 5 \mu m$, $L = 1 \mu m$) was isolated using an SF₆ reactive ion etching

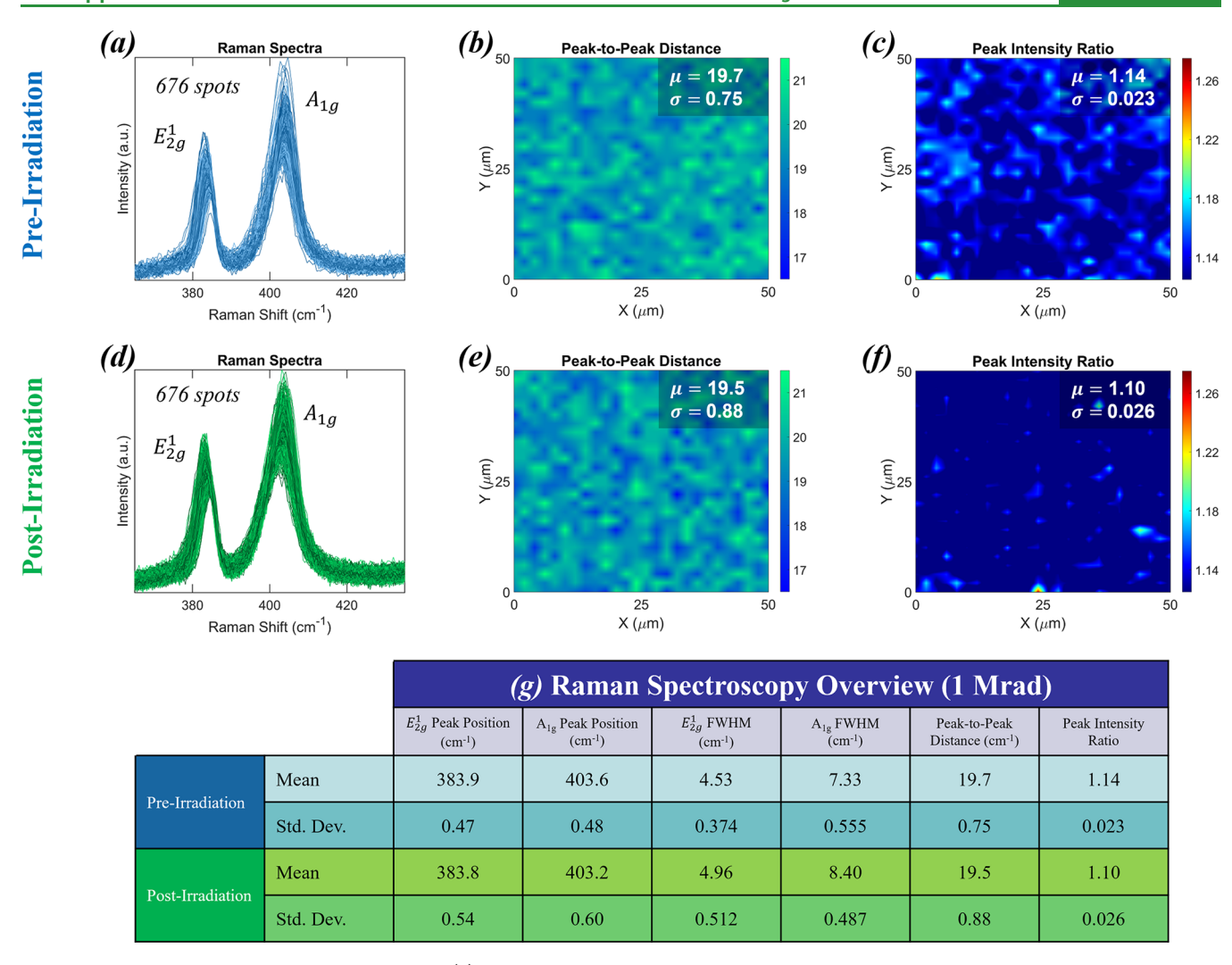


Figure 3. Raman spectroscopy of monolayer MoS₂. (a) Pre-irradiation Raman spectra of the monolayer MoS₂ film used in this study taken with a 532 nm laser at 676 points over a 50 μ m × 50 μ m area. The in-plane E_{2g}^{-1} and out-of-plane A_{1g} active modes are labeled. Spatial colormaps of (b) peak-to-peak distance and (c) peak intensity ratio for the Raman spectra shown in (a). Insets at the top right corner of the colormaps denote the mean (μ) and standard deviation (σ) for each parameter. (d) Post-irradiation Raman spectra of the monolayer MoS₂ film taken at 676 points over another 50 μ m × 50 μ m area. Spatial colormaps of (e) peak-to-peak distance and (f) peak intensity ratio for the Raman spectra shown in (a). (g) Table overviewing the parameters extracted from the pre- and post-irradiation Raman spectra. A slight (<0.5 cm⁻¹) redshift was noted for the mean E_{2g}^{-1} and A_{1g} peak locations following irradiation. The full width at half maximum (FWHM) of both active modes also increased. However, the large standard deviation of these results compared to the magnitude of the observed changes indicates low statistical significance, making it difficult to draw a concrete conclusion.

(RIE), and source/drain electrodes (40 nm Ni and 30 nm Au) were deposited using e-beam evaporation. Interconnects (60 nm Ni and 40 nm Au) were added between neighboring devices in a subsequent lithography step to create circuits. An optical image of the full 1 cm \times 1 cm substrate containing over 1500 2D MoS₂ memtransistors used in this study is shown in Figure 1c; the devices on the substrate were split into separate groups to ensure accurate extraction of device characteristics as they pertain to baseline performance (computing), sensing, and memory. Gamma irradiation of the substrate was performed using 60 Co as the γ -ray source, with the emitted photons possessing energies of 1.17 and 1.33 MeV. At these energies, photon-matter interaction primarily takes the form of Compton scattering, 8,28 in which incident high-energy photons collide with stationary electrons and impart energy to them before being scattered as lower energy photons in different directions. If the energy imparted is sufficiently high, the electrons are ejected from their positions and become

energetic free electrons; this causes the formation of electronhole pairs which may recombine elsewhere, become trapped in defect (trap) sites, or be collected at an electrode. It is important to note that the energetic free electrons produced through these interactions undergo subsequent charged particle interactions within the material, with these secondary interactions being the primary energy transfer method from the initial photons to the material, causing many more excitation and ionization events. Additionally, unlike photon interactions, these interactions are capable of imparting sufficient energy to atoms to displace them and create defects. A diagram of the irradiation setup used for this study is shown in Figure 1d,e. The irradiation chamber used was a lead-shielded cylinder with a diameter of ~6 in. and a height of 8 in. Multiple ⁶⁰Co sources were arrayed around the chamber. To ensure a uniform dose rate and TID for all devices, a custom-designed, paper-based sample fixture was used to suspend the sample within the center of the irradiation chamber, allowing for minimal

shielding of gamma radiation for a dose rate of $\sim 160 \text{ krad/h}$ and a TID of 1 Mrad. The dose rate and TID administered to the sample were both determined using a detector located within the irradiation chamber. See the Methods section for further details on the MoS_2 synthesis, film transfer, device/circuit fabrication, and irradiation setup.

A scanning electron microscopy (SEM) image of a representative 2D MoS₂ memtransistor is seen in Figure 2a. Furthermore, scanning transmission electron microscopy (STEM) was used to investigate the structure of the transferred MoS₂ film used in this study and verify its quality. The same transfer technique mentioned previously was used to transfer the as-grown film from its sapphire growth substrate to a TEM grid. A high-angle annular dark-field (HAADF)-STEM image taken at an 80 kV accelerating voltage is presented in Figure 2b, showing the atomic structure of the MoS₂ film viewed down its c-axis. It can be clearly seen that the transferred film possesses a crystalline 2H-MoS₂ structure with little-to-no point defects, establishing that the transfer process is relatively damage-free and thus has minimal impact on the device performance discussed further on. This is supported by the selected area electron diffraction (SAED) results shown in Figure 2c, which show a uniform single-crystalline structure. Cross-sectional TEM was used to affirm the integrity of the back-gate dielectric stack following irradiation, with an image of a representative memtransistor being shown in Figure 2d. Additionally, energy-dispersive X-ray spectroscopy (EDS) was used to analyze the elemental distribution of the stack, with the results being shown in Figure 2e. A clear line of Mo and S atoms indicates that the MoS₂ film remained coherent throughout irradiation, while the distribution of Al and Hf shows a clear delineation between the Al₂O₃ tunneling/ blocking layers and the HfO2 charge-trapping layer. These results confirm that the channel and back-gate stack were not subjected to any major structural alterations as a result of the irradiation.

PL and Raman maps were used to assess the quality of the MoS₂ film before and after irradiation; all maps were taken with a 532 nm laser on the same substrate used for memtransistor fabrication. Figure S1a,b shows the preirradiation PL spectra and corresponding spatial colormap of the A excitonic peak location taken across 676 points over a 50 $\mu m \times 50 \mu m$ area. Insets at the top right corner of the colormaps denote the mean (μ) and standard deviation (σ) for each parameter. High uniformity was noted with a mean A excitonic peak position of 1.82 eV, which is indicative of monolayer MoS₂. Figure S1c₂d shows the post-irradiation PL spectra and corresponding spatial colormap of the A excitonic peak location. A redshift in the mean A excitonic peak position from 1.82 to 1.80 eV was noted following irradiation and may indicate a reduction in the band gap of MoS₂ due to tensile strain,³⁸ potentially stemming from the introduced sulfur vacancies. While this shift exceeds the spectral resolution of the PL measurements (3 \times 10⁻⁴ eV), thus indicating statistical significance, shifts of similar or greater magnitude may also be induced by environmental factors;³⁹ as the sample was irradiated in an ambient environment, correlation of the PL results with additional material characterization (i.e., Raman spectroscopy) is necessary for determining the significance of the observed shift.

To validate these results and provide additional insight, Raman spectroscopy was also conducted before and after irradiation using the same parameters as PL spectroscopy.

Figure 3a-c, respectively, shows the pre-irradiation Raman spectra and corresponding spatial colormaps of peak-to-peak separation and peak intensity ratio between the E_{2g}^{-1} (in-plane) and A_{1g} (out-of-plane) active modes of MoS₂ taken at 676 points over the same 50 μ m \times 50 μ m area studied using PL. Spatial colormaps of peak location and full width at halfmaximum (FWHM) for the E_{2g}^{-1} and A_{1g} peaks prior to irradiation are found in Figure S2a-d. Insets at the top right corner of the colormaps denote the mean (μ) and standard deviation (σ) for each parameter. The mean E_{2g}^{-1} and A_{1g} peak locations were found to be 383.9 and 403.6 cm⁻¹, respectively, with a mean peak separation of 19.7 cm⁻¹ and a mean peak intensity ratio of 1.14. Additionally, the mean FWHM was found to be 4.53 cm⁻¹ for the E_{2g}^{-1} peak and 7.33 cm⁻¹ for the A_{1g} peak. Following irradiation, Raman spectroscopy was again conducted using the same parameters and in the same general vicinity used to obtain the pre-irradiation results. Note that there was little-to-no overlap between the locations of the preand post-irradiation measurements. The post-irradiation Raman spectra and corresponding spatial colormaps of peakto-peak separation and peak intensity ratio between the $E_{2\sigma}^{-1}$ and A_{1g} active modes are shown in Figure 3d-f, while spatial colormaps of peak location and FWHM are shown in Figure S2e-g. A slight (<0.5 cm⁻¹) redshift was noted for the mean E_{2g}^{-1} and A_{1g} peak locations (383.8 and 403.2 cm⁻¹, respectively), though the mean peak separation and peak intensity ratio remained relatively unchanged at 19.5 cm⁻¹ and 1.10, respectively. The FWHM of both active modes was also found to noticeably increase to 4.96 cm⁻¹ for the E_{2g}^{-1} peak and $8.44~{\rm cm}^{-1}$ for the A_{1g} peak. Similar phenomena were reported by Shakya *et al.*⁴⁰ following the bombardment of MoS₂ nanosheets with swift heavy ions at low fluences. They attributed this to phonon confinement arising from localized bond stretching (tensile strain) near defect sites, potentially supporting our initial observations of vacancy generation and strain from the PL spectra. A summary of the pre-and postirradiation Raman spectroscopy results is shown in Figure 3g. Notably, the large standard deviation of our results compared to the magnitude of the observed changes indicates low statistical significance, making it difficult to draw a concrete conclusion. Together, the PL and Raman spectroscopy results indicate that the pre-irradiation MoS₂ film is both uniform and of high quality and that, while there may be a slight increase in defect density due to irradiation-induced damage, the magnitude of radiation impact appears low even at a TID of 1 Mrad, with little-to-no effect on film uniformity and quality. As the post-irradiation shift in the Raman spectra is on the order of the spectral resolution (~0.5 cm⁻¹), the radiation impact cannot be held as statistically significant despite the apparent significance of the change in the PL peak position (0.02 eV with a spectral resolution of $\sim 3 \times 10^{-4}$ eV); these changes are no more extreme than what can be expected to occur in large-area MoS2 if it is exposed to air for the same amount of time as it took for irradiation to be completed and may even be artifacts induced by the laser used during spectroscopy.³⁹ While prior studies on gamma irradiation of MoS_2 have reported a blueshift in the post-irradiation E_{2g}^{-1} and A_{1g} peaks of the Raman spectra, $a_{1g}^{8,28}$ it is important to note that most of these studies were conducted at higher TIDs than the 1 Mrad utilized in this work. From the work of Singh and Singh,²⁸ a blueshift in the Raman spectra of monolayer MoS₂ can only be seen when the TID exceeds ~5 Mrad; conversely, at a TID of 1 Mrad, little-to-no change is seen in the Raman

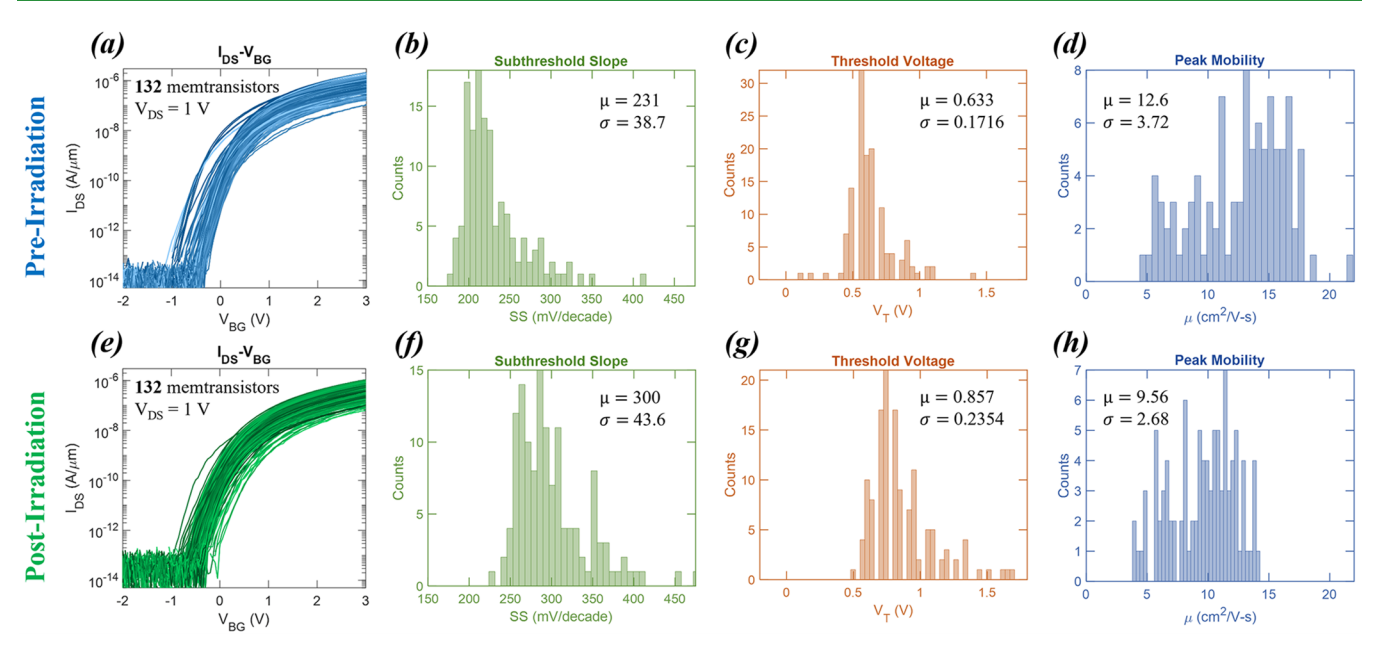


Figure 4. Gamma radiation hardness of 2D MoS₂ memtransistors. (a) Transfer characteristics, *i.e.*, source-to-drain current (I_{DS}) as a function of the local back-gate voltage (V_{BG}) , at a source-to-drain voltage (V_{DS}) of 1 V for 132 as-fabricated 2D MoS₂ memtransistors with channel lengths (L) of 1 μ m and channel widths (W) of 5 μ m. Histograms of (b) subthreshold slope (SS) and (c) threshold voltage (V_{th}) extracted from the memtransistors shown in (a). (d) Histogram of peak field-effect mobility (μ_{FE}) extracted from a separate set of 100 memtransistors. μ_{FE} was extracted using the peak transconductance method; this was performed separately from the SS and V_{th} extractions due to the need for the devices to be pushed to a higher overdrive voltage than those achieved in (a) in order to prevent μ_{FE} from being underestimated. Insets denote the mean (μ) and standard deviation (σ) for each parameter. (e) Transfer characteristics of the same 132 2D MoS₂ memtransistors shown in (a) following gamma irradiation at a TID of 1 Mrad. Histograms of (f) SS and (g) V_{th} extracted from the post-irradiation memtransistors shown in (e). (h) Histogram of μ _{FE} extracted from the same memtransistors as in (e) following irradiation. A clear increase in mean SS and shift in mean V_{th} can be seen, indicating the generation/filling of trap states at the MoS₂/Al₂O₃ interface and deep in the back-gate dielectric stack. Additionally, an approximately 25% decrease in μ _{FE} indicates the generation of defects (scattering sites) in the MoS₂ channel and a corresponding decrease in the time between scattering events.

spectra, which is in close agreement with our results. While Isherwood *et al.*⁸ noted a slight blueshift of both the Raman and PL spectra at a TID of 4 Mrad, their Raman spectroscopy results were expressly noted to be statistically insignificant, and the accompanying PL spectroscopy results could not be correlated with them.

Figure 4a shows the pre-irradiation transfer characteristics, i.e., source-to-drain current (I_{DS}) vs back-gate voltage (V_{BG}) , of 132 MoS₂ memtransistors taken at a drain voltage (V_{DS}) of 1 V. The back-gate voltage was swept from 3 to -2 V in steps of 50 mV and back. Minimal hysteresis can be seen, denoting a lack of interfacial trap states in the as-fabricated devices. Figure 4b,c shows histograms of SS and V_{th} , respectively, extracted from the characteristics shown in Figure 4a. A histogram of $\mu_{\rm FE}$ for 100 MoS₂ memtransistors is shown in Figure 4d. μ_{FE} was extracted using the peak transconductance method; this was performed separately from the SS and $V_{
m th}$ extractions due to the need for the devices to be pushed to a higher overdrive voltage to prevent $\mu_{\rm FE}$ from being underestimated. An independent set of devices was used to prevent non-volatile programming of the devices, as will be discussed later. The mean (μ) and standard deviation (σ) for each parameter are listed in their respective histograms. ON/OFF ratios of $>10^6$, a mean SS of ~231 mV/decade, a mean $V_{\rm th}$ of ~0.633 V, and a mean $\mu_{\rm FE}$ of ~12.6 cm²/Vs indicate that the as-fabricated devices were of high quality and relatively free of defects and oxide traps. Following irradiation, the same devices tested in Figure 4a-d were again electrically characterized. Figure 4e shows the post-irradiation transfer characteristics of the 132 MoS_2 memtransistors shown in Figure 4a-c taken at $V_{DS} = 1$

V. Histograms of SS and $V_{\rm th}$ extracted from the transfer characteristics of the irradiated devices are shown in Figure 4f,g. The mean SS was found to be ~300 mV/decade, and the mean $V_{\rm th}$ was found to be ~0.857 V. Clearly, a slight increase in mean SS (Δ SS) of 69 mV/decade and a shift in mean $V_{\rm th}$ ($\Delta V_{\rm th}$) of 0.224 V are noted in the irradiated devices when compared to the as-fabricated devices. These changes can be easily explained using eqs 1 and 2

$$SS = 2.3 \frac{k_{\rm B}T}{q} \left(1 + \frac{C_{\rm D} + C_{\rm IT}}{C_{\rm OX}} \right)$$
 (1)

$$\Delta V_{\rm th} = -\frac{\Delta Q_{\rm IT}}{C_{\rm OY}} - \frac{\Delta Q_{\rm F}}{C_{\rm OY}} \tag{2}$$

Here, $C_{\rm OX}$ is the oxide capacitance, $k_{\rm B}$ is the Boltzmann constant, T is the temperature, q is the charge of an electron, $C_{\rm D}$ is the depletion capacitance, $C_{\rm IT}$ is the interface trap capacitance, $\Delta Q_{\rm IT}$ is the change in interface charge, and $\Delta Q_{\rm F}$ is the change in (fixed) charge trapped in the oxide. Note that $C_{\rm D}$ is often neglected when considering 2D TMDC-based transistors due to their ultra-thin body and fully depleted channels. From eqs 1 and 2, it is readily apparent that the accumulation of charges at the interface or deep in the oxide will lead to an increase in SS and a shift in $V_{\rm th}$. As stated previously, gamma radiation is a form of ionizing radiation, providing sufficient energy to excite electrons and generate electron—hole pairs. These charges may then fill vacant trap states, preventing recombination and leading to the effects described in eqs 1 and 2 and seen in Figure 4f,g. As $\Delta V_{\rm th}$ is

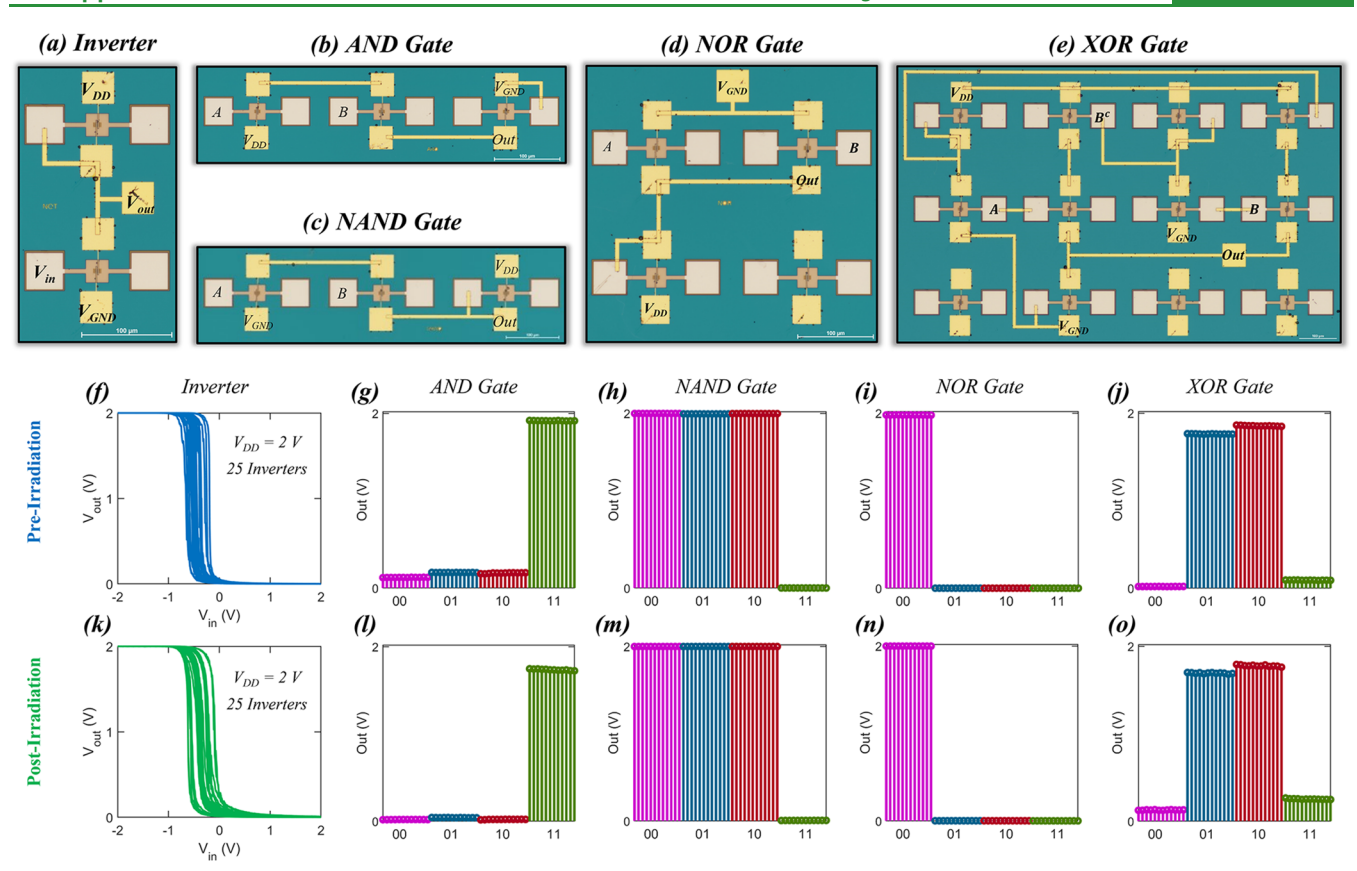


Figure 5. Gamma radiation hardness of logic gates created using 2D MoS₂ memtransistors. Optical images of a representative (a) NOT gate (inverter), (b) AND gate, (c) NAND gate, (d) NOR gate, and (e) XOR gate created using 2D MoS2 memtransistors as their base unit. Asfabricated input-output results of (f) inverters, (g) AND gates, (h) NAND gates, (i) NOR gates, and (j) XOR gates. All gates tested were able to successfully perform their desired logic operations, indicating the suitability of 2D MoS₂ memtransistors for more complex circuit architectures. Also note that the inverter results shown in (f) are taken for 25 distinct inverters, indicating that any inherent device-to-device variation does not impede logic functionality. Post-irradiation input-output results of (k) inverters, (l) AND gates, (m) NAND gates, (n) NOR gates, and (o) XOR gates. While there was a slight change in the post-irradiation logic states, all gates remained able to successfully perform their desired logic operations, indicating the suitability of our MoS₂ memtransistors for complex, radiation-hard circuit architectures.

positive, the trapped charges must be predominantly negative (electrons). Interestingly, as the dependencies of SS and $\Delta V_{\rm th}$ differ, with SS depending solely on interface charges while ΔV_{th} depends on both oxide and interface charges, it is possible to identify the impact of the irradiation on both areas. A simple calculation using eq 1 indicates a meager $\sim 1.4 \times$ increase in C_{IT} as compared to the measurements taken preirradiation. Figure 4h shows a histogram of μ_{FE} for the same devices as in Figure 4d following irradiation. The mean $\mu_{\rm FE}$ was found to be ~9.56 cm²/Vs, a decrease of ~3.04 cm²/Vs from the pre-irradiation statistics. This was taken to indicate the generation of defects (scattering sites) in the MoS₂ channel, leading to a reduction in the time between scattering events $(\tau_{\rm s})$ and a reduction in $\mu_{\rm FE}$ via the relation $\mu_{\rm FE}=rac{q au_{
m s}}{m_{
m eff}}$, where $m_{\rm eff}$ is the charge carrier effective mass. While these results seem to support the hypothesized defect (sulfur vacancy) formation indicated by the post-irradiation PL and Raman spectra, it is important to note that the relative change in $\mu_{\rm FE}$ is ultimately quite small. Previous studies of carrier mobility following ion irradiation have shown that large-scale defect formation results in an order of magnitude change in $\mu_{\rm FE}$. 19,20,22 The results shown here thus indicate that the defect density does not appreciably increase following gamma irradiation at a TID of 1 Mrad, which supports our earlier observations that the changes in the PL and Raman spectra are

statistically insignificant and that there was a negligible change in the uniformity/quality of the MoS₂ film. Negative-bias temperature instability (NBTI) tests were also conducted on the MoS₂ memtransistors before and after irradiation to investigate the impact of a 1 Mrad TID on device reliability, with the results being shown in Figure S3. Representative devices were held at a $V_{\rm BG}$ of $-3~{
m V}$ for stress times $(t_{
m stress})$ of 1, 10, 100, and 1000 s, consecutively, while at room temperature (25 °C) and at 125 °C. The transfer characteristics, taken at $V_{\rm DS}$ = 1 V, for each stress condition, are shown in Figure S3a,b for the pre- and post-irradiated devices, respectively. Figure S3c shows a plot of the change in $V_{\rm th}$ ($\Delta V_{\rm th}$) vs $t_{\rm stress}$ at 25 and 125 °C for both the pre- and post-irradiated devices. Little difference in $\Delta V_{\rm th}$ trends can be seen for the pre- and postirradiated devices at the temperatures tested, indicating that the overall reliability of the MoS₂ memtransistors was not severely impacted by a TID of 1 Mrad.

The viability of our MoS₂ memtransistors for large-scale integrated circuits has been demonstrated by their implementation in various logic functionalities, including NOT gates (inverters), AND gates, NAND gates, NOR gates, and XOR gates. Optical images of these circuits are shown in Figure 5ae, while their input-output results are shown in Figure 5f-j, respectively. A three-stage cascaded inverter was also developed using our MoS2 memtransistors, with its optical

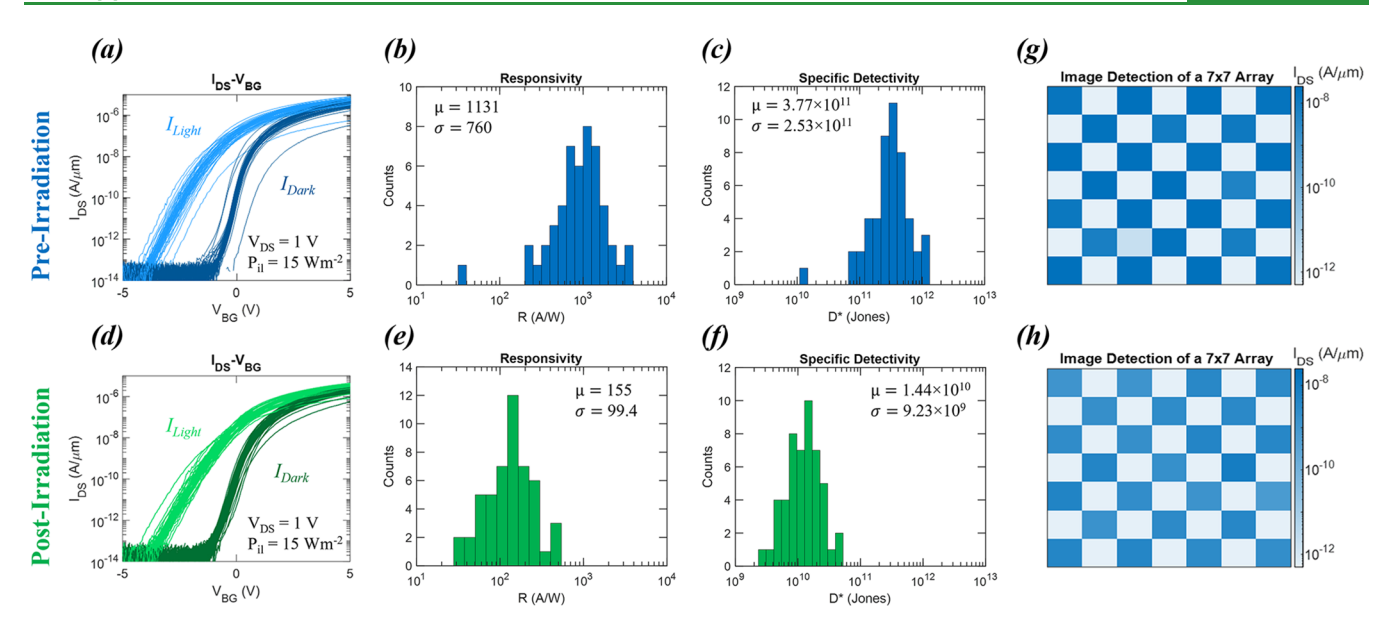


Figure 6. Gamma radiation hardness of photosensing in 2D MoS₂ memtransistors. (a) Transfer characteristics at $V_{\rm DS}=1$ V for 50 as-fabricated 2D MoS₂ memtransistors before (dark blue) and during (light blue) exposure to white light with an illumination power density ($P_{\rm il}$) of 15 Wm⁻². The shift in $V_{\rm th}$ between the dark current ($I_{\rm dark}$) and the light current ($I_{\rm light}$) is indicative of the photogating effect, *i.e.*, a screening of the electric field across the channel by trapped photogenerated carriers. Histograms of (b) responsivity (R) and (c) detectivity (D^*) extracted from the transfer characteristics shown in (a) at $V_{\rm BG}=-1$ V. Insets denote the mean (μ) and standard deviation (σ) for each parameter. R is used to gauge the conversion efficiency of a photodetector, while D^* is a geometry/bandwidth-independent metric for assessing photodetector performance. (d) Transfer characteristics at $V_{\rm DS}=1$ V for 50 2D MoS₂ memtransistors in the dark and under illumination after gamma irradiation at a TID of 1 Mrad. Histograms of (e) R and (f) D^* extracted from the transfer characteristics shown in (d) at $V_{\rm BG}=-1$ V. Due to the degradation in SS and shift in $V_{\rm th}$ apparent between (a) and (d), the mean R and D^* are both shown to decrease by approximately one order of magnitude. Photodetection of a checkerboard pattern using a 7 × 7 memtransistor array (g) before and (h) after irradiation. Despite the reduction in R and D^* following irradiation, the pattern was able to be accurately detected in both cases, indicating that the photosensing capabilities of 2D MoS₂ memtransistors were not significantly affected at TIDs up to 1 Mrad.

image, circuit schematic, and input-output results being shown in Figure S4a-c, respectively. As can be seen, all gates tested were able to successfully perform their desired logic operations, indicating the suitability of our MoS2 memtransistors for more complex circuit architectures. Additionally, the representative inverter, AND gate, NAND gate, NOR gate, and XOR gate shown in Figure 5f-j were found to operate with average power budgets of 1.45 nW, 3.88 nW, 418 pW, 1.91 nW, and 1.42 nW, respectively; these results demonstrate the suitability of MoS2-memtransistor-based logic circuits for low-power edge environments. The logic functionalities of these gates were also assessed following gamma irradiation in order to determine their resistance to TID effects that may cause logic upsets. The input-output results of the same circuits shown in Figure 5f-j are given in Figure 5k-o following a TID of 1 Mrad. The post-irradiation input-output results of the three-stage cascaded inverter are shown in Figure S4c. While there was a slight change in the post-irradiation logic states, all gates tested were able to successfully perform their desired logic operations both before and after irradiation, indicating the suitability of our MoS2 memtransistors for complex, radiation-hard circuit architectures.

To provide insight into the photosensing performance (photoresponse) of MoS_2 memtransistors, the transfer characteristics of 50 representative devices were taken in the dark and under illumination with an illumination power density $(P_{\rm il})$ of 15 W/m². The results for this test when conducted at $V_{\rm DS}=1$ V are shown in Figure 6a. A diffuse white light was chosen for demonstrating photoresponse due to its

simulation of a more realistic lighting condition than the lasers used in most contemporary studies. The P_{il} for the light used in this study was calibrated against a commercially available silicon PIN photodiode. The absorption of the incident light, which occurs so long as the photon energy (E_{ph}) is larger than the bandgap of the MoS₂ channel ($E_g \approx 1.8$ eV), causes the generation of electron/hole pairs as electrons in the valence band are excited to the conduction band. While these carriers would otherwise recombine, the presence of a lateral electric field due to an applied bias $(V_{\rm DS})$ causes them to be swept to the source/drain electrodes and collected. This results in an apparent increase in the conductivity of the channel, which is reflected by an increase in the light current (I_{light}) as compared to the dark current (I_{dark}). The difference between I_{light} and I_{dark} is referred to as the photocurrent (I_{ph}) and is often used to evaluate the photoresponse of a device. It is also important to note the shift in the $V_{\rm th}$ of the memtransistors when they are exposed to light. This is indicative of photogating effects, i.e., trapping of photogenerated carriers, and is regularly observed in conjunction with photoconduction during the operation of MoS₂ transistors under illumination. 41,42 The photoresponses of the MoS₂ memtransistors demonstrated in Figure 6a were evaluated according to several notable figures of merit for photodetectors. Responsivity (R), measured in AW^{-1} , is the ratio between $I_{\rm ph}$ and the total incident optical power seen by the photodetector, representing the conversion efficiency between input signals and output signals. It is given by eq 3

$$R = \frac{I_{\rm ph}}{P_{\rm il} \times A} \tag{3}$$

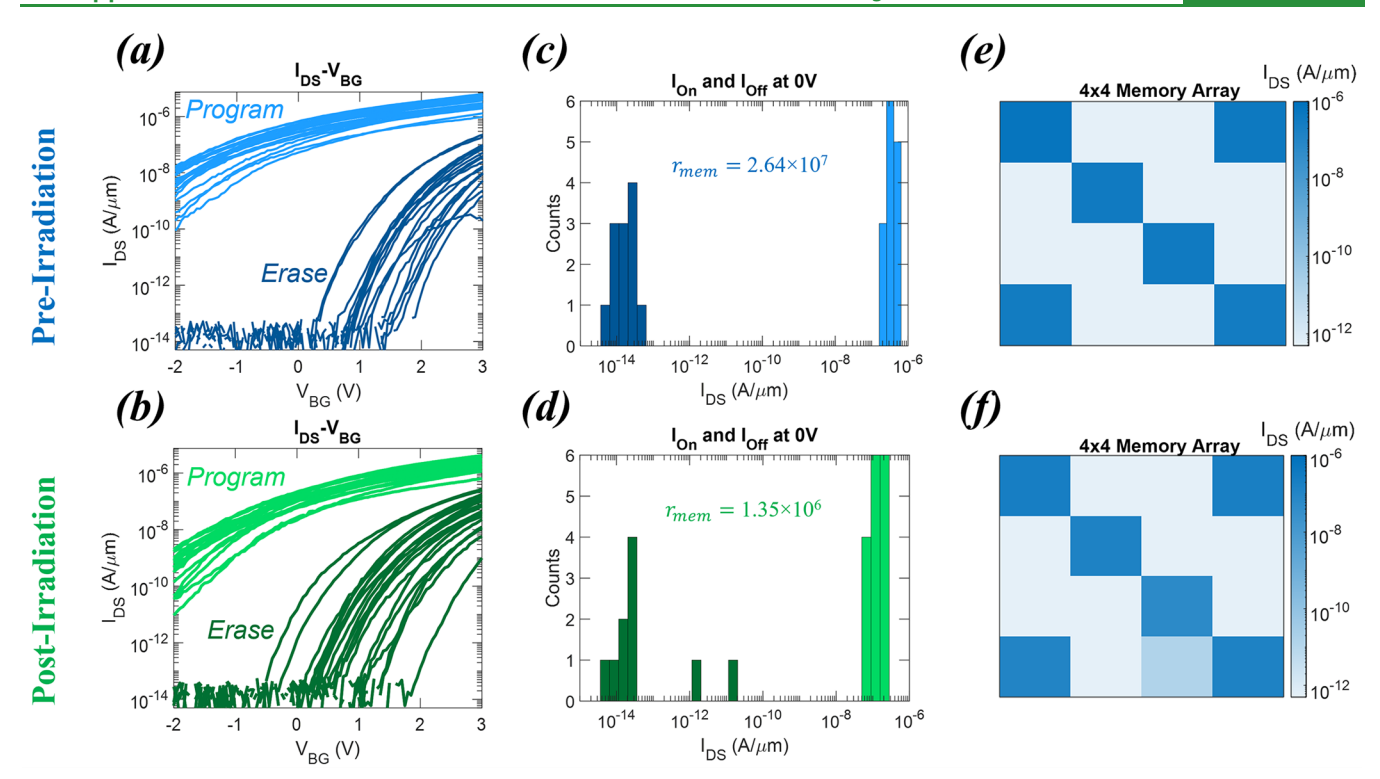


Figure 7. Gamma radiation hardness of memory in 2D MoS₂ memtransistors. (a) Transfer characteristics at $V_{\rm DS}=1$ V for 20 as-fabricated 2D MoS₂ memtransistors after a programming back-gate bias ($V_{\rm program}$) pulse of -10 V (light curves) and after an erasing back-gate bias ($V_{\rm erase}$) pulse of +12 V (dark curves). The pulse time ($t_{\rm pulse}$) for both cases was 100 ms. (b) Transfer characteristics at $V_{\rm DS}=1$ V for the program/erase states of the 20 2D MoS₂ memtransistors shown in (a) after gamma irradiation at a TID of 1 Mrad. Histograms of the current extracted at $V_{\rm BG}=0$ V for the program/erase states (c) before and (d) after irradiation. The mean ratio between the two memory states ($r_{\rm mem}$) is given for both cases and is shown to have decreased by approximately one order of magnitude following irradiation. Storage of an arbitrary pattern in a 4 × 4 memtransistor array (e) before and (f) after irradiation. Despite the change in $r_{\rm mem}$ following irradiation, the stored memory states remain easily distinguishable, indicating that the memory capabilities of 2D MoS₂ memtransistors remain effective at TIDs up to and exceeding 1 Mrad.

where I_{ph} is the photocurrent of the photodetector extracted at $V_{\rm BG} = -1$ V and $V_{\rm DS} = 1$ V, $P_{\rm il}$ is the illumination power density of the light source in $W/\mu m^2$, and $A = 5 \mu m^2$ is the area of the photoactive channel. Figure 6b shows a histogram of R for all 50 devices shown in Figure 6a, with the mean R being a respectable ~1131 A/W. Higher R-values can be achieved by extracting $I_{\rm ph}$ at different $V_{\rm BG}$, making comparisons with other photodetectors difficult. Hence, consideration of other metrics is typically needed to make fair comparisons between photodetectors. A major limiting factor in photodetector design is the total background noise (ambient, intrinsic, etc.) seen by the device. The noise equivalent power (NEP) of a photodetector is a measurement of the minimum illumination (signal) power capable of being detected through this noise, i.e., the minimum power at which the signal-to-noise ratio is unity at 1 Hz bandwidth, and is given by eq 4

$$NEP = \frac{I_{\text{noise}}}{R} \tag{4}$$

where $I_{\rm noise}$ is the noise current density (in A Hz^{-1/2}) in the dark at 1 Hz bandwidth and R is the responsivity. For this study, $I_{\rm noise} = 6.7 \times 10^{-13}$ A Hz^{-1/2} and 2.4×10^{-12} A Hz^{-1/2} was extracted from the 1/f noise of a representative MoS₂ memtransistor before and after irradiation, respectively. Using NEP, one can then derive the specific detectivity (D^*) of a photodetector using eq 5

$$D^* = \frac{\sqrt{A}}{\text{NEP}} \tag{5}$$

where A is the active area of the device. This is a popular metric for assessing/comparing photodetector performance as it excludes any influences from a device's geometry and bandwidth on its sensitivity. Figure 6c shows a histogram of D^* for all 50 devices shown in Figure 6a,b, with the mean D* being a respectable 3.77×10^{11} Jones. To assess the impact of gamma irradiation on the photosensing performance of MoS₂ memtransistors, 50 fresh (i.e., uncharacterized) devices were characterized following a TID of 1 Mrad; this was purposefully chosen to avoid non-volatile photogating effects from the pre-irradiation characterization. 43,44 Electrical characterization noted similar trends to the post-irradiation devices shown in Figure 4e-h, indicating that the results are consistent with our previous discussion. The transfer characteristics of the postirradiation devices are shown in Figure 6d for the same illumination conditions as in Figure 6a, while histograms of R and D* for the devices are shown in Figure 6e.f. An approximately one order of magnitude decrease can be noted in mean R and D^* following irradiation. This is primarily attributed to the degradation in SS and shift in $V_{\rm th}$ noted earlier, as these factors place the extraction voltage $(V_{BG} = -1)$ V) within the subthreshold region of the irradiated devices; this, in turn, leads to a relative decrease in I_{ph} and thus R and D*. These effects can be mitigated to some extent by tuning the $V_{\rm BG}$ at which R and D^* are extracted. For instance, as shown in Figure S5, extracting the post-irradiation R at a more positive $V_{\rm BG}$ ($V_{\rm BG} \approx 0$ V) allows for a recovery to the preirradiation values extracted at $V_{\rm BG}$ = -1 V. However, we do note that the peak R value attainable for a given memtransistor

does decrease following irradiation; this may be a result of the reduction in mean $\mu_{\rm FE}$, which would result in lower current values at a given overdrive voltage following irradiation. Recovery of D^* is more difficult as I_{noise} increases with I_{dark} in the subthreshold region and ON-state, causing D^* to decrease further in those regimes. While these changes are significant, the image detection capabilities of MoS₂ memtransistors were not found to be severely impacted, as demonstrated in Figure 6g,h. A 7×7 array of MoS₂ memtransistors were used to capture a checkerboard pattern based on their response to illumination. The results for the pre- and post-irradiation devices are shown in Figure 6g,h, respectively, for I_{DS} extracted at $V_{\rm BG}$ = -0.9 V. As can be easily seen, the pattern was able to be detected in both cases, indicating that a TID of 1 Mrad did not significantly affect image detection capabilities. The average power consumption for each memtransistor in the array was found to be ~15.8 nW; even if each memtransistor in the array experienced a detection event, the overall power consumption would be <800 nW. While already promising, the power consumption of the memtransistors can be further tuned for more power-constrained applications/environments by extracting at different $V_{\rm BG}$.

The memory capabilities of our MoS₂ memtransistors, as enabled by their Al₂O₃/HfO₂/Al₂O₃ gate stack, were investigated prior to and following irradiation. The origin of these capabilities can be easily explained using the band diagram shown in Figure S6. The Al₂O₃/HfO₂/Al₂O₃ gate dielectric stack enables NVM in MoS2-based memtransistors by allowing the trapping/detrapping of charge carriers in the HfO₂ (charge-trapping) layer when bias pulses of sufficient magnitude are applied to the back-gate. The polarity of the pulse determines which charge carriers are trapped/detrapped, with holes (electrons) being trapped when negative (positive) pulses are applied and vice versa. These trapped charges screen the electric field across the MoS2 channel, changing the conductance of the device and allowing for the realization of distinct conductance (memory) states. Figure 7a,b shows the transfer characteristics ($V_{\rm DS}$ = 1 V) of 20 memtransistors before and after a 1 Mrad TID, respectively. The lighter curves denote the high conductance ON-states achieved by applying a 100 ms negative bias pulse ($V_{\rm program}$) of magnitude 10 V to the back-gate of each device, while the darker curves denote the low conductance OFF-states subsequently achieved by applying a 100 ms positive bias pulse $(V_{\rm erase})$ of magnitude 12 V. As demonstrated by the band diagram shown in Figure S6, applying a large $V_{\rm program}$ pulse allows holes to tunnel across the 7 nm Al₂O₃ tunneling layer and become trapped in the 3 nm HfO₂ charge-trapping layer, where they screen the electric field across the MoS2 channel and provoke a negative shift in V_{th} and an increase in conductance. Subsequently applying a large V_{erase} pulse allows the trapped holes to tunnel out of the trapping layer and allows electrons to tunnel in, positively shifting $V_{\rm th}$ and lowering conductance. Note that, while the biases applied during programming/erasing are large, the energy expenditure of each programming/erasing event $(E_{P/E})$ is quite small. $E_{P/E}$ can be calculated using eq 6

$$E_{P/E} = V_{DS} \int_0^{\tau_{\text{pulse}}} I_{DS}(t) dt + \frac{1}{2} C_{OX} V_{P/E}^2$$
(6)

where $V_{\rm DS}$ and $I_{\rm DS}$ are the source-to-drain voltage and current, respectively, during the pulsing operation, au_{pulse} is the pulse width, $V_{P/E}$ is the program/erase bias applied to the back-gate, and C_{OX} is the oxide (back-gate) capacitance. As V_{DS} is kept at 0 V during each program/erase operation, the first term of eq 6 can be safely ignored, and $E_{P/E}$ can be approximated as

$$E_{\rm P/E} \approx \frac{1}{2} C_{\rm OX} V_{\rm P/E}^{2} \tag{7}$$

Using eq 7, $E_{P/E}$ was found to be <0.7 pJ even for erasing operations where $V_{\text{erase}} = +12 \text{ V}$, indicating high energy efficiency. Figure 7c,d contains histograms of the I_{DS} extracted from the transfer characteristics shown in Figure 7a,b, respectively, at $V_{\rm BG}$ = 0 V. The mean memory ratio $(r_{\rm mem})$ between the ON-OFF states was found to be 2.64×10^7 for the as-fabricated devices and 1.35×10^6 for the same devices exposed to a 1 Mrad TID. While a one order of magnitude decrease in r_{mem} is significant, a memory ratio of >10⁶ remains relevant for information storage applications. This is illustrated by the storage of the pattern shown in Figure 7e,f for a 4 × 4 memory array before and after irradiation, respectively. Littleto-no change can be seen, demonstrating that the ON-states of the MoS₂ memtransistors remain distinct enough from their OFF-states for information to be reliably stored and accessed. The endurance and retention of the MoS₂ memtransistors were also assessed before and after irradiation, with the results for a representative device being shown in Figure S7. Figure S7a,b shows the endurance of the device over 50 program/ erase cycles ($V_{\text{program}} = -10 \text{ V}$, $V_{\text{erase}} = +12 \text{ V}$, and $t_{\text{pulse}} = 100 \text{ V}$ ms) before and after irradiation, respectively. In both cases, little-to-no degradation in the memory ratio between the ONstate and the OFF-state was seen during the cycling, indicating good endurance and minimal radiation impact. Note that, while an initial degradation in memory ratio can be seen at the beginning of cycling, this is likely an artifact of performing endurance testing following all other memory characterization; the full memory ratio could be restored by applying a larger program/erase bias pulse. The retention of the device over a period of \sim 600 s, read at a constant $V_{\rm DS}$ of 1 V, is shown in Figure S7c,d for the as-fabricated device and for the same device following irradiation, respectively. Little-to-change can be seen between the two cases, indicating that the memory retention of the MoS₂ memtransistors was not severely impacted by a TID of 1 Mrad.

DISCUSSION

In conclusion, we have assessed the potential of 2D MoS₂ memtransistors for realizing radiation resilient edge devices by exploring their sensing, computing, and storage capabilities, both as fabricated and after irradiation at a TID of 1 Mrad. First, the transfer characteristics of >100 devices were investigated, with the mean SS, V_{th} , and μ_{FE} experiencing only a slight degradation after irradiation and NBTI testing demonstrating that the memtransistor reliability was not severely impacted by TID effects. Various logic gates were fabricated using MoS₂ memtransistors as their constituent elements; the logic functionalities of these gates were largely unaltered by irradiation, indicating their radiation hardness. Next, the sensing capabilities of 100 memtransistors were assessed on the basis of their responsivity and specific detectivity to optical stimuli. While the mean responsivity and detectivity were found to degrade, the ratio between the light and dark currents remained significant enough to permit accurate image capture and identification. Finally, testing of the memory (storage) capabilities of MoS₂ memtransistors saw minimal change in their memory retention and endurance post-irradiation; while the impact on memory ratio was more

substantial, memory states remained distinct and differentiable from one another. Together, these results demonstrate the high-performance and gamma radiation resilience of MOCVDgrown MoS₂ memtransistors for multiple functionalities, even in the absence of dedicated radiation shielding and mitigation techniques. We believe that this work may serve as a steppingstone in the development of all-in-one sensing, computing, and storage edge devices/platforms for radiationheavy environments such as deep space and nuclear facilities; there remains significant room for application-oriented study in this field, such as dedicated in situ gamma irradiation experimentation, that will offer further insight into device performance in these extreme environments.

METHODS

Large-Area Monolayer MoS₂ Film Growth. Monolayer MoS₂ was deposited on an epi-ready 2" c-sapphire substrate by MOCVD. An inductively heated graphite susceptor equipped with wafer rotation in a cold-wall horizontal reactor was used to achieve uniform monolayer deposition. Molybdenum hexacarbonyl (Mo(CO)₆) and hydrogen sulfide (H₂S) were used as precursors. Mo(CO)₆ maintained at 25 °C and 375 Torr in a stainless-steel bubbler was used to deliver 2.0×10^{-2} sccm of the metal precursor for the growth, while 400 sccm of H₂S was used for the process. MoS₂ deposition was carried out at 950 °C and 50 Torr in H2 ambient, with monolayer growth being achieved in 18 min. Prior to growth, the substrate was baked at 1000 $^{\circ}\text{C}$ in H_2 for 10 min. Following growth, the substrate was cooled in H₂S to 300 °C to inhibit the decomposition of the MoS₂ film. More details on the growth process can be found in earlier works. 35,36

Fabrication of Local Back-Gate Islands. To define the backgate island regions, a commercially purchased substrate (thermally grown 285 nm SiO₂ on p⁺⁺-Si) was spin-coated at 4000 rpm for 45 s with a bilayer photoresist consisting of lift-off resist (LOR 5A) and series photoresist (SPR 3012); following application, these resists were baked at 185 °C for 120 s and 95 °C for 60 s, respectively. The bilayer photoresist was then patterned using a Heidelberg maskless aligner (MLA 150) to define the islands and developed by immersing the substrate in MF CD26 microposit for 75 s, followed by a 60 s deionized (DI) water rinse. The back-gate electrodes of 20/50 nm Ti/Pt were then deposited using e-beam evaporation in a Temescal FC-2000 Bell Jar Deposition System. Lift-off of the remaining photoresist and excess metal was achieved using acetone and photo resist stripper (PRS 3000); the substrate was then cleaned using 2-propanol (IPA) and DI water. An ALD process was then implemented to grow the back-gate dielectric stack consisting of 40 nm Al_2O_3 ($\varepsilon_{ox}\approx 10$), 3 nm HfO_2 ($\varepsilon_{ox} \approx 25$), and 7 nm Al_2O_3 across the entire substrate, including the island regions; all ALD processes were conducted at 200 °C and without breaking vacuum. Access to the individual Pt backgate electrodes was achieved via an RIE process conducted in a Plasma-Therm Versalock 700. First, etch patterns were defined using the same bilayer photoresist (LOR 5A and SPR 3012) used previously. The bilayer photoresist was again exposed using an MLA 150 and developed using MF CD26 microposit with a DI water rinse. The dielectric stack was then dry etched using BCl3 RIE chemistry at 5 °C for 80 s; this process was split into four 20 s etch steps separated by 60 s stabilization steps to minimize heating in the substrate. Finally, the photoresist was removed using the same process described earlier for liftoff.

MoS₂ Film Transfer to the Local Back-Gate Island Substrate. Film transfer from the growth substrate to the application substrate was performed using a polymethyl methacrylate (PMMA)-assisted wet transfer process.³⁷ First, the as-grown MoS₂ on the sapphire substrate was spin-coated with PMMA and left to sit for 24 h to ensure good PMMA/MoS2 adhesion. The corners of the spin-coated film were then scratched using a razor blade and immersed inside a 2 M NaOH solution kept at 90 °C. Capillary action caused the NaOH to be preferentially drawn into the substrate/MoS₂ interface, owing to

the hydrophilic nature of sapphire and the hydrophobic nature of MoS₂ and PMMA, separating the PMMA/MoS₂ stack from the sapphire substrate. The separated film was then fished from the NaOH solution using a clean glass slide and rinsed in three separate water baths for 15 min each before finally being transferred onto the application substrate. Subsequently, the substrate was baked at 50 and 70 °C for 10 min each to remove moisture and promote film adhesion, thus ensuring a pristine interface, before the PMMA was removed by immersing the sample in acetone for 1 h, and the substrate was cleaned with a subsequent 30 min IPA bath.

Fabrication of 2D MoS₂ Transistors. To define the channel regions of the MoS₂ transistors discussed in this work, the application substrate, with MoS₂ transferred on top, was spin-coated with PMMA A6 (4000 rpm for 45 s) and baked at 180 °C for 90 s. The resist was then exposed using a Raith EBPG5200 e-beam lithography tool and developed using a 1:1 mixture of 4-methyl-2-pentanone (methyl isobutyl ketone, MIBK) and IPA (60 s) and then rinsed using IPA (45 s). The exposed monolayer MoS₂ film was subsequently etched using a sulfur hexafluoride (SF₆) RIE process at 5 °C for 30 s. Next, the sample was rinsed in acetone and IPA to remove the e-beam resist. A subsequent lithography step was conducted to form source/drain electrodes. The substrate was spin-coated at 4000 rpm for 45 s with methyl methacrylate (MMA) EL6 and PMMA A3; following application, these resists were baked at 150 °C for 90 s and 180 °C for 90 s, respectively. E-beam lithography was again used to pattern the source and drain, and development was again performed using a 1:1 mixture of MIBK/IPA and an IPA rinse for the same times as previously. 40 nm of Ni and 30 nm of gold (Au) were deposited using e-beam evaporation to form the electrodes. Finally, a lift-off process was performed to remove the excess Ni/Au by immersing the sample in acetone for 1 h, followed by IPA for another 30 min to clean the substrate. At this stage, each island contains one MoS2 transistor to allow for individual gate control of each device.

Integration of 2D MoS₂ Memtransistors to Form Logic Gates. To define the connections between individual transistors for circuit creation, the substrate was first spin-coated at 4000 rpm for 45 s with MMA EL11 and PMMA A3 and baked at 150 °C for 90 s and 180 $^{\circ}\text{C}$ for 90 s, respectively. Note that this bilayer resist differs from that used previously to define the source/drain electrodes; MMA EL11 is thicker at these spin/bake conditions than MMA EL6, allowing for the deposition of a thicker metal layer without risking sidewall coverage. The bilayer resist was then patterned using e-beam lithography and developed using the same 1:1 MIBK/IPA and IPA rinse processes mentioned previously. E-beam evaporation was performed to deposit 60 nm Ni and 40 nm Au, forming the connections between neighboring devices; a thicker metal layer was deposited at this step to ensure the continuity of the connections over the features defined in previous lithography steps. Finally, the e-beam resist and excess metal were rinsed away in a lift-off process using acetone (1 h) and IPA (30 min).

Irradiation Conditions. Irradiation of the as-fabricated devices was conducted in an ambient environment at the Breazeale Nuclear Reactor, a part of the Radiation Science and Engineering Center (RSEC) at the Pennsylvania State University. 1.173 and 1.332 MeV photons (γ -rays) were emitted from 60 Co, a common isotope used in testing gamma radiation hardness for space qualification.^{7,8} The irradiation chamber used was a lead-shielded cylinder with a diameter of ~6 in. and a height of 8 in. Multiple 60Co sources were arrayed around the chamber in a pool of demineralized water. To ensure a uniform dose rate and TID for all devices, a cardboard sample holder was used to suspend the sample within a 4 in. \times 4 in. \times 4 in. cube at the center of the irradiation chamber, regarded as the isodose region. In this region, a dose rate of ~160 krad/h was maintained up to a TID of 1 Mrad. The overall uncertainty of the absorbed dose rate in the chamber was ±2.4% at a 95% confidence level, as measured and certified under NIST's National Voluntary Laboratory Accreditation Program (NVLAP) using the Fricke dosimetry system.

Scanning and Transmission Electron Microscopy. SEM of the 2D MoS₂ memtransistors used in this study was conducted using a Zeiss Gemini 500 field emission scanning electron microscopy

(FESEM) system at an accelerating voltage of 5 kV. HAADF-STEM was performed using an aberration-corrected ThermoFisher Titan³ G2 60-300 system with a monochromator and X-field emission gun source at an accelerating voltage of 80 kV. The convergence semiangle used for STEM imaging was 30.0 mrad, and the collection angle range of the HAADF detector was 42-244 mrad. The SAED spot pattern was collected using a ThermoFisher Talos F200X system at an accelerating voltage of 200 kV. Cross-sectional TEM was performed using the same ThermoFisher Talos F200X system on a representative 2D MoS₂ memtransistor prepared using a Helios NanoLab 660 focused ion beam system with a 30 kV Ga ion beam. A sacrificial layer of carbon was deposited over the memtransistor via ebeam followed by ion-beam-assisted deposition in order to protect the 2D MoS₂ prior to milling and transferring the cross-section to a TEM grid for final thinning and polishing with a 5 kV Ga ion beam. The Talos F200X was used to collect EDS maps of the memtransistor's cross-section.

Raman and PL Spectroscopy. Raman spectroscopy and PL spectroscopy of the pre- and post-irradiation MoS_2 film were performed on a Horiba LabRAM HR Evolution confocal Raman microscope with a 532 nm laser. The power was 34 mW filtered at 5% to 1.7 mW. The objective magnification was $100\times$ with a numerical aperture of 0.9, and the grating had a spacing of 1800 g/mm for Raman and 300 g/mm for PL. The spectral resolution of each Raman and PL measurement was approximately 0.5 cm⁻¹ and 3×10^{-4} eV, respectively. Each Raman and PL measurement was taken from a single accumulation with a dwell time of 0.5 s.

Electrical Characterization. Electrical characterization of the fabricated devices was performed in a Lake Shore CRX-VF probe station under atmospheric conditions using a Keysight B1500A parameter analyzer. Pre-irradiation electrical characterization of the MoS_2 -based memtransistors was performed within 24 h of the start of gamma irradiation. Post-irradiation electrical characterization was performed within 24 h of receiving the irradiated sample from RSEC. All measurements were completed within 8 h of the initial measurement. No appreciable shift in electrical performance was noted between the first and last sets of measurements.

ASSOCIATED CONTENT

5 Supporting Information

The Supporting Information is available free of charge at https://pubs.acs.org/doi/10.1021/acsami.3c02406.

PL spectroscopy characterization of monolayer MoS₂ before and after irradiation; Raman spectroscopy trends in monolayer MoS₂ before and after irradiation; impact of gamma radiation on 2D MoS₂ memtransistor reliability; 3-stage cascaded inverters based on MoS₂ memtransistors before and after a TID of 1 Mrad; responsivity (R) before and after irradiation; band diagram of the Al₂O₃/HfO₂/Al₂O₃ gate dielectric stack; and further memory characterization of MoS₂ memtransistors before and after a TID of 1 Mrad (PDF)

AUTHOR INFORMATION

Corresponding Author

Saptarshi Das — Engineering Science and Mechanics, Materials Science and Engineering, Applied Research Laboratory, 2D Crystal Consortium Materials Innovation Platform, Materials Research Institute, and Electrical Engineering and Computer Science, Penn State University, University Park, Pennsylvania 16802, United States; Orcid.org/0000-0002-0188-945X; Email: sud70@psu.edu, das.sapt@gmail.com

Authors

Thomas F. Schranghamer – Engineering Science and Mechanics, Penn State University, University Park, Pennsylvania 16802, United States

Andrew Pannone – Engineering Science and Mechanics, Penn State University, University Park, Pennsylvania 16802, United States

Harikrishnan Ravichandran – Engineering Science and Mechanics, Penn State University, University Park, Pennsylvania 16802, United States

Sergei P. Stepanoff – Materials Science and Engineering and Applied Research Laboratory, Penn State University, University Park, Pennsylvania 16802, United States

Nicholas Trainor – Materials Science and Engineering and 2D Crystal Consortium Materials Innovation Platform, Materials Research Institute, Penn State University, University Park, Pennsylvania 16802, United States

Joan M. Redwing — Materials Science and Engineering and 2D Crystal Consortium Materials Innovation Platform, Materials Research Institute, Penn State University, University Park, Pennsylvania 16802, United States; orcid.org/0000-0002-7906-452X

Douglas E. Wolfe – Engineering Science and Mechanics, Materials Science and Engineering, Applied Research Laboratory, and Nuclear Engineering, Penn State University, University Park, Pennsylvania 16802, United States

Complete contact information is available at: https://pubs.acs.org/10.1021/acsami.3c02406

Author Contributions

All authors contributed to the preparation of the manuscript. **Notes**

The authors declare no competing financial interest. The datasets generated during and/or analyzed during the current study are available from the corresponding author upon reasonable request. The codes used for plotting the data are available from the corresponding authors on reasonable request.

ACKNOWLEDGMENTS

This work was funded by the Department of Defense, Defense Threat Reduction Agency (DTRA), as part of the Interaction of Ionizing Radiation with Matter University Research Alliance (IIRM-URA) under contract number HDTRA1-20-2-0002. The content of the information does not necessarily reflect the position or the policy of the federal government, and no official endorsement should be inferred. This work was also supported by the National Science Foundation (NSF) through the Career Award under grant number ECCS-2042154. The authors also acknowledge the materials support from the NSF through the Pennsylvania State University 2D Crystal Consortium—Materials Innovation Platform (2DCC-MIP) under NSF cooperative agreement DMR-2039351.

REFERENCES

- (1) Shi, W.; Dustdar, S. The Promise of Edge Computing. *Computer* **2016**, 49, 78–81.
- (2) Hung, J.-M.; Li, X.; Wu, J.; Chang, M.-F. Challenges and Trends in Developing Nonvolatile Memory-Enabled Computing Chips for Intelligent Edge Devices. *IEEE Trans. Electron Devices* **2020**, *67*, 1444–1453.
- (3) Xue, C.-X.; Chiu, Y.-C.; Liu, T.-W.; Huang, T.-Y.; Liu, J.-S.; Chang, T.-W.; Kao, H.-Y.; Wang, J.-H.; Wei, S.-Y.; Lee, C.-Y.; Huang,

- S.-P.; Hung, J.-M.; Teng, S.-H.; Wei, W.-C.; Chen, Y.-R.; Hsu, T.-H.; Chen, Y.-K.; Lo, Y.-C.; Wen, T.-H.; Lo, C.-C.; Liu, R.-S.; Hsieh, C.-C.; Tang, K.-T.; Ho, M.-S.; Su, C.-Y.; Chou, C.-C.; Chih, Y.-D.; Chang, M.-F. A CMOS-Integrated Compute-in-Memory Macro based on Resistive Random-Access Memory for AI Edge Devices. *Nat. Electron.* **2020**, *4*, 81–90.
- (4) Gupta, A.; Jha, R. K. A Survey of 5G Network: Architecture and Emerging Technologies. *IEEE Access* **2015**, *3*, 1206–1232.
- (5) Sharma, P. K.; Park, J.; Park, J. H.; Cho, K. Wearable Computing for Defence Automation: Opportunities and Challenges in 5G Network. *IEEE Access* **2020**, *8*, 65993–66002.
- (6) Prinzie, J.; Simanjuntak, F. M.; Leroux, P.; Prodromakis, T. Low-Power Electronic Technologies for Harsh Radiation Environments. *Nat. Electron.* **2021**, *4*, 243–253.
- (7) Vogl, T.; Sripathy, K.; Sharma, A.; Reddy, P.; Sullivan, J.; Machacek, J. R.; Zhang, L.; Karouta, F.; Buchler, B. C.; Doherty, M. W.; Lu, Y.; Lam, P. K. Radiation Tolerance of Two-Dimensional Material-Based Devices for Space Applications. *Nat. Commun.* **2019**, 10, 1202–1210.
- (8) Isherwood, L. H.; Athwal, G.; Spencer, B. F.; Casiraghi, C.; Baidak, A. Gamma Radiation-Induced Oxidation, Doping, and Etching of Two-Dimensional MoS₂ Crystals. *J. Phys. Chem. C* **2021**, 125, 4211–4222.
- (9) Sebastian, A.; Pendurthi, R.; Choudhury, T. H.; Redwing, J. M.; Das, S. Benchmarking Monolayer MoS₂ and WS₂ Field-Effect Transistors. *Nat. Commun.* **2021**, *12*, 693–712.
- (10) Das, S.; Sebastian, A.; Pop, E.; McClellan, C. J.; Franklin, A. D.; Grasser, T.; Knobloch, T.; Illarionov, Y.; Penumatcha, A. V.; Appenzeller, J.; Chen, Z.; Zhu, W.; Asselberghs, I.; Li, L.-J.; Avci, U. E.; Bhat, N.; Anthopoulos, T. D.; Singh, R. Transistors Based on Two-Dimensional Materials for Future Integrated Circuits. *Nat. Electron.* **2021**, *4*, 786–799.
- (11) Wang, L.; Chen, L.; Wong, S. L.; Huang, X.; Liao, W.; Zhu, C.; Lim, Y.-F.; Li, D.; Liu, X.; Chi, D.; Ang, K.-W. Electronic Devices and Circuits Based on Wafer-Scale Polycrystalline Monolayer MoS₂ by Chemical Vapor Deposition. *Adv. Electron. Mater.* **2019**, *5*, 1900393.
- (12) Subbulakshmi Radhakrishnan, S.; Chakrabarti, S.; Sen, D.; Das, M.; Schranghamer, T. F.; Sebastian, A.; Das, S. A Sparse and Spike-Timing-Based Adaptive Photoencoder for Augmenting Machine Vision for Spiking Neural Networks. *Adv. Mater.* **2022**, *34*, 2202535.
- (13) Jayachandran, D.; Oberoi, A.; Sebastian, A.; Choudhury, T. H.; Shankar, B.; Redwing, J. M.; Das, S. A Low-Power Biomimetic Collision Detector Based on an In-Memory Molybdenum Disulfide Photodetector. *Nat. Electron.* **2020**, *3*, 646–655.
- (14) Dodda, A.; Oberoi, A.; Sebastian, A.; Choudhury, T. H.; Redwing, J. M.; Das, S. Stochastic Resonance in MoS₂ Photodetector. *Nat. Commun.* **2020**, *11*, 4406–4411.
- (15) Li, J.; Zhang, H.; Ding, Y.; Li, J.; Wang, S.; Zhang, D. W.; Zhou, P. A Non-Volatile AND Gate Based on Al₂O₃/HfO₂/Al₂O₃ Charge-Trap Stack for In-Situ Storage Applications. *Sci. Bull.* **2019**, *64*, 1518–1524
- (16) Shen, J.; Zhou, B.; Wang, F.; Wan, Q.; Shan, X.; Li, C.; Lin, X.; Zhang, K. Low Consumption Two-Terminal Artificial Synapse Based on Transfer-Free Single-Crystal MoS₂ Memristor. *Nanotechnology* **2020**, *31*, 265202.
- (17) Zhang, S.; Liu, Y.; Zhou, J.; Ma, M.; Gao, A.; Zheng, B.; Li, L.; Su, X.; Han, G.; Zhang, J.; Shi, Y.; Wang, X.; Hao, Y. Low Voltage Operating 2D MoS_2 Ferroelectric Memory Transistor with $Hf_{1-x}Zr_xO_2$ Gate Structure. Nanoscale Res. Lett. **2020**, 15, 157–159.
- (18) Dodda, A.; Trainor, N.; Redwing, J. M.; Das, S. All-in-One, Bio-Inspired, and Low-Power Crypto Engines for Near-Sensor Security Based on Two-Dimensional Memtransistors. *Nat. Commun.* **2022**, *13*, 3587–3612.
- (19) Arnold, A. J.; Shi, T.; Jovanovic, I.; Das, S. Extraordinary Radiation Hardness of Atomically Thin MoS₂. ACS Appl. Mater. Interfaces **2019**, 11, 8391–8399.
- (20) Ochedowski, O.; Marinov, K.; Wilbs, G.; Keller, G.; Scheuschner, N.; Severin, D.; Bender, M.; Maultzsch, J.; Tegude, F. J.; Schleberger, M. Radiation Hardness of Graphene and MoS₂ Field

- Effect Devices against Swift Heavy Ion Irradiation. J. Appl. Phys. 2013, 113, 214306.
- (21) Zhang, Y.; Chen, X.; Wang, H.; Dai, J.; Xue, J.; Guo, X. Electronic Properties of Multilayer MoS₂ Field Effect Transistor with Unique Irradiation Resistance. *J. Phys. Chem. C* **2021**, *125*, 2089–2096.
- (22) Smyth, C. M.; Cain, J. M.; Lang, E. J.; Lu, P.; Yan, X.; Liu, S. E.; Yuan, J.; Bland, M. P.; Madden, N. J.; Ohta, T.; Sangwan, V. K.; Hersam, M. C.; Hattar, K.; Chou, S. S.; Lu, T.-M. Resilience of Monolayer MoS₂ Memtransistor under Heavy Ion Irradiation. *J. Mater. Res.* 2022, 37, 2723–2737.
- (23) Li, H.; Liu, C.; Zhang, Y.; Qi, C.; Wei, Y.; Zhou, J.; Wang, T.; Ma, G.; Tsai, H.-S.; Dong, S.; Huo, M. Electron Radiation Effects on the Structural and Electrical Properties of MoS₂ Field Effect Transistors. *Nanotechnology* **2019**, *30*, 485201.
- (24) Giubileo, F.; Iemmo, L.; Passacantando, M.; Urban, F.; Luongo, G.; Sun, L.; Amato, G.; Enrico, E.; Di Bartolomeo, A. Effect of Electron Irradiation on the Transport and Field Emission Properties of Few-Layer MoS₂ Field-Effect Transistors. *J. Phys. Chem. C* **2019**, 123, 1454–1461.
- (25) Lu, M.-Y.; Wu, S.-C.; Wang, H.-C.; Lu, M.-P. Time-Evolution of the Electrical Characteristics of MoS₂ Field-Effect Transistors after Electron Beam Irradiation. *Phys. Chem. Chem. Phys.* **2018**, 20, 9038–9044.
- (26) Kim, T.-Y.; Cho, K.; Park, W.; Park, J.; Song, Y.; Hong, S.; Hong, W.-K.; Lee, T. Irradiation Effects of High-Energy Proton Beams on MoS₂ Field Effect Transistors. *ACS Nano* **2014**, *8*, 2774–2781.
- (27) Huang, X.-n.; Shi, J.-y.; Yao, Y.; Peng, S.-a.; Zhang, D.-y.; Jin, Z. Layer Thickness Influenced Irradiation Effects of Proton Beam on MoS₂ Field Effect Transistors. *Nanotechnology* **2021**, *32*, 135204.
- (28) Singh, A.; Singh, R. γ-ray Irradiation-Induced Chemical and Structural Changes in CVD Monolayer MoS₂. ECS J. Solid State Sci. Technol. **2020**, 9, 093011.
- (29) He, Y.; Xiang, X.; Wu, Z.; Li, M.; Deng, H.; Zhang, J.; Yang, G.; Chen, H.; Yuan, Y.; Zu, X. γ -Ray Dose Dependent Conductivity of MoS₂ Nanomaterials at Different Temperatures. *CrystEngComm* **2019**, 21, 6830–6837.
- (30) Özden, A.; Ay, F.; Sevik, C.; Perkgöz, N. K. CVD Growth of Monolayer MoS₂: Role of Growth Zone Configuration and Precursors Ratio. *Jpn. J. Appl. Phys.* **2017**, *56*, 06GG05.
- (31) Chen, D.; Li, J.; Wei, Z.; Wei, X.; Zhu, M.; Liu, J.; Zhang, G.; Zhang, Z.; Chen, J.-H. Repairable Polymer Solid Electrolyte Gated MoS₂ Field Effect Devices with Large Radiation Tolerance. *Adv. Electron. Mater.* **2022**, *8*, 2100619.
- (32) Benton, E. R.; Benton, E. V. Space Radiation Dosimetry in Low-Earth Orbit and Beyond. *Nucl. Instrum. Methods Phys. Res., Sect. B* **2001**, *184*, 255–294.
- (33) Zhang, E.; Wang, W.; Zhang, C.; Jin, Y.; Zhu, G.; Sun, Q.; Zhang, D. W.; Zhou, P.; Xiu, F. Tunable Charge-Trap Memory Based on Few-Layer MoS2. *ACS Nano* **2015**, *9*, 612–619.
- (34) Wali, A.; Ravichandran, H.; Das, S. A Machine Learning Attack Resilient True Random Number Generator Based on Stochastic Programming of Atomically Thin Transistors. *ACS Nano* **2021**, *15*, 17804–17812.
- (35) Xuan, Y.; Jain, A.; Zafar, S.; Lotfi, R.; Nayir, N.; Wang, Y.; Choudhury, T. H.; Wright, S.; Feraca, J.; Rosenbaum, L.; Redwing, J. M.; Crespi, V.; van Duin, A. C. Multi-Scale Modeling of Gas-Phase Reactions in Metal-Organic Chemical Vapor Deposition Growth of WSe₂. J. Cryst. Growth 2019, 527, 125247.
- (36) Xiang, Y.; Sun, X.; Valdman, L.; Zhang, F.; Choudhury, T. H.; Chubarov, M.; Robinson, J. A.; Redwing, J. M.; Terrones, M.; Ma, Y.; Gao, L.; Washington, M. A.; Lu, T.-M.; Wang, G.-C. Monolayer MoS₂ on Sapphire: An Azimuthal Reflection High-Energy Electron Diffraction Perspective. 2D Materials 2021, 8, 025003.
- (37) Sebastian, A.; Zhang, F.; Dodda, A.; May-Rawding, D.; Liu, H.; Zhang, T.; Terrones, M.; Das, S. Electrochemical Polishing of Two-Dimensional Materials. *ACS Nano* **2018**, *13*, 78–86.

- (38) Conley, H. J.; Wang, B.; Ziegler, J. I.; Haglund, R. F.; Pantelides, S. T.; Bolotin, K. I. Bandgap Engineering of Strained Monolayer and Bilayer MoS₂. *Nano Lett.* **2013**, *13*, 3626–3630.
- (39) Subramanian, S.; Briggs, N.; Shallenberger, J.; Wetherington, M. T.; Robinson, J. A. Caveats in Obtaining High-Quality 2D Materials and Property Characterization. *J. Mater. Res.* **2020**, *35*, 855–863.
- (40) Shakya, J.; Kumar, S.; Kanjilal, D.; Mohanty, T. Work Function Modulation of Molybdenum Disulfde Nanosheets by Introducing Systematic Lattice Strain. *Sci. Rep.* **2017**, *7*, 9576.
- (41) Di Bartolomeo, A.; Genovese, L.; Foller, T.; Giubileo, F.; Luongo, G.; Croin, L.; Liang, S.-J.; Ang, L. K.; Schleberger, M. Electrical Transport and Persistent Photoconductivity in Monolayer MoS₂ Phototransistors. *Nanotechnology* **2017**, *28*, 214002.
- (42) Nur, R.; Tsuchiya, T.; Toprasertpong, K.; Terabe, K.; Takagi, S.; Takenaka, M. High Responsivity in MoS₂ Phototransistors Based on Charge Trapping HfO₂ Dielectrics. *Commun. Mater.* **2020**, *1*, 103–109.
- (43) Zheng, Y.; Ravichandran, H.; Schranghamer, T. F.; Trainor, N.; Redwing, J. M.; Das, S. Hardware Implementation of Bayesian Network Based on Two-Dimensional Memtransistors. *Nat. Commun.* **2022**, *13*, 5578–5611.
- (44) Dodda, A.; Jayachandran, D.; Pannone, A.; Trainor, N.; Stepanoff, S. P.; Steves, M. A.; Radhakrishnan, S. S.; Bachu, S.; Ordonez, C. W.; Shallenberger, J. R.; Redwing, J. M.; Knappenberger, K. L.; Wolfe, D. E.; Das, S. Active Pixel Sensor Matrix Based on Monolayer MoS₂ Phototransistor Array. *Nat. Mater.* **2022**, *21*, 1379–1387.